IOP Conf. Series: Materials Science and Engineering **274** (2017) 012007 doi:10.1088/1757-899X/274/1/012007

Effect of pre-strain on precipitation and exfoliation corrosion resistance in an Al-Zn-Mg alloy

Xianghan Lu [1], Zhiwei Du [2], Xiaolei Han [2], Ting Li [2], Guojun Wang [3], Liying Lu [3], Xiaoxia Bai [3] and Tietao Zhou [1,*]

[1]School of Materials Science and Engineering, Beihang University, Beijing 100191, China.
[2]National Analysis and Testing Center for Nonferrous Metals & Electronic Materials, Beijing General Research Institute for Nonferrous Metals, Beijing 100088, China 3.
[3]Northeast Light Alloy Co., Ltd., Harbin 150060, China.

*Corresponding author e-mail: 04380@buaa.edu.cn

Abstract. To investigate the effect of pre-strain on behaviors in a specially developed Al-4.5Zn-1.2Mg alloy, transmission electron microscopy (TEM) bright field (BF) imaging combined with select area electron diffraction (SAED), Vickers-hardness tests and electrical conductivity tests was conducted for insight into precipitation in aluminum (Al) matrix during two step ageing, and standard exfoliation corrosion (EXCO) test combined with high-angle angular dark field scanning transmission electron microscopy (HAADF-STEM) and scanning electron microscopy (SEM) was carried out for corrosion behavior. Results showed that pre-strain accelerated precipitation during two step ageing as the sequence of: (i) supersaturated solid solution (SSS), GPI zones precipitations, GPI dissolution; (ii) SSS, fcc precipitates, η' phases or η phases. And the precipitation hardening of the fcc precipitates was not effective as GPI zones. Pre-strain also accelerated EXCO developing, which was mainly attributed to the coverage ratio of η phases on high-angle grain boundaries (HAGBs) increasing as pre-strain increase.

1. Introduction

Precipitation hardened Al-Zn-Mg alloys, known as 7xxx series aluminum alloys, are widely used as structural materials in constructions, vehicles and aircrafts due to high specific strength, toughness as well as good formability[1,2,3]. Compared with other 7xxx series aluminum alloys, the specially developed Al-Zn-Mg alloy used in this study contains lower Zn, Mg, and Cu to obtain higher ductility, better weld ability, and corrosion resistance as a sacrifice of some strength [4, 5, and 6]. Precipitation and corrosion resistance are therefore deemed critical behaviors in this Al-Zn-Mg alloy, reflecting performance and durability in applications.

In precipitation hardened Al-Zn-Mg alloys, quenching from the solution heat treatment temperature is an inevitable step to acquire high strength and uniform properties [7, 8]. However, this step is bound to high thermal gradients in materials, which is the cause of high magnitude residual stresses, even inhomogeneous plastic deformation[7] and distortions during machining of large and complex parts[9,10]. Considering degrading original behaviors at minimum, applying pre-strain after quenching

is better to avoid the harm of residual stresses in semi-finished aluminum alloy products, compared to reducing quench rate [7].

So far, according to the paper published[11,12], productions and computer simulations were conducted to investigate quench-induced residual stresses relieving by applying pre-strain, showing 1-3% uniform pre-strain in the rolling direction eliminated most stresses without much strain-hardening. With the in-depth research, it was found that the behaviors of Al alloys varied with pre-strain applied, see for example D. Wang(2009)[13], N. M. Han(2011)[14]. As shown in former works that effects of pre-strain on behaviors were composition-varying [14, 15, 16, 17] or heat treatment-varying [13, 14], critical behaviors (like precipitation and corrosion resistance [18]) shall be therefore tested if the alloys are aimed at application.

This work aimed to investigate precipitation and EXCO resistance that were presented in 12mm thick Al-Zn-Mg plates, where the main experimental variable was the pre-strain after quenching. The two step ageing were conducted on these plates, since several former works had reported excellent improvement on corrosion resistance by this ageing treatment [19, 20, 21, and 22]. Precipitation was investigated mainly by TEM combined with Vickers-hardness and electrical conductivity tests. The EXCO resistance results were collected under the standard of ASTM G34 [23], which is commonly used on 7xxx series Al alloys. And SEM, electron back-scattered diffraction (EBSD) and HAADF-STEM, which were verified as effective method to investigate EXCO resistance in our former work, were used for further investigation.

2. Experimental

2.1. Material and heat treatment

In this work, the specially developed 12mm-thick Al-4.5Zn-1.2Mg alloy plate containing small amounts of Mn, Cr, Cu and Zr was supplied in hot-rolled condition. Five plates numbered as A, B, C, D and E were stretched after solution treatment at 470℃ for 1h and followed room temperature water quench at the rate of 2mm/min till about 0%, 0.65%, 1.97%, 3.41% and 7.50% strain, respectively. Then the several samples with different size were cut from the five plates for further investigations. These samples were aged at 95℃ for 24h firstly and at 160℃ for periods of 0h-4h afterward.

2.2. Vicker-hardness and electrical conductivity test

The Vickers-hardness (5kg load) and the electrical conductivity of the samples with different pre-strain and ageing treatment at 160℃ for periods of 0h, 0.5h, 1h, 1.5h, 2h, 2.5h, 3h, 3.5h and 4h were measured at room temperature.

2.3. EXCO test

The EXCO tests were performed on the five samples undergone complete two step ageing according to the standard EXCO test as described in ASTM G34-2001(2013)[23]. The EXCO test solution whose chemical composition of 4 mol/L sodium chloride, 0.5 mol/L potassium nitrate and 0.1 mol/L nitric acid was maintained 25℃±3℃ during whole test. After 48h of continuous immersion in the EXCO test solution, corrosion morphology was recorded by camera, and the susceptibility to EXCO was determined by visual examination with performance ratings established by reference to standard photographs N (No obvious attack), P (pits, sometimes with a tendency for undercutting and slight lifting of metal around the pits), EA (tiny blisters, thin chips, flakes or powder, companied with only slight separation of metal) and EB to ED (range from moderate penetration into the metal to much more considerable penetration and loss of metal).

2.4. Microstructural examination

Samples were cut from the samples after the Vickers-hardness and electrical conductivity tests or EXCO test for further study on microstructure. SEM observations were performed on longitudinal sections using JSM-6510 scanning electron microscope after mirror polishing. JSM-7001F scanning

electron microscope and Edax Pegasus XM2 EBSD accessories were used for EBSD observations on longitudinal sections of different samples to analyze and calculate fraction of recrystallization and HAGBs. The samples for these observations and calculations were prepared by electrolytic polishing. SAED patterns, matrix precipitates and precipitates on HAGB were studied by TEM, HAADF-STEM on Tecnai G2 F20 transmission electron microscope and high-resolution (HR-) TEM on JEOL-2010 transmission electron microscope. The thin foils for TEM and HAADF-STEM were prepared by mechanical grinding and final twin-jet electro polishing in the solution of 25% nitric acid and 75% methanol at about -35℃.

3. Results

The electrical conductivity test is an effective method to analyze precipitation in Al matrix [24]. As shown in Fig.1, the electrical conductivity in all samples increases during 0h to 0.5h of the second stage ageing, sustaining at above 20.0MS/m until 1h, while the peak of this stage cannot be measured precisely. Then, the electrical conductivity in pre-strained samples decreases rapidly and soon rises up from 1h to 2.5h, compared to durative decrease in the sample A without pre-strain. After 2.5h, the conductivity of all the samples increases until the second stage ageing finished. Compared to the higher pre-strained sample D and E, the electrical conductivities in the sample A, B and C are lower during the second step ageing.

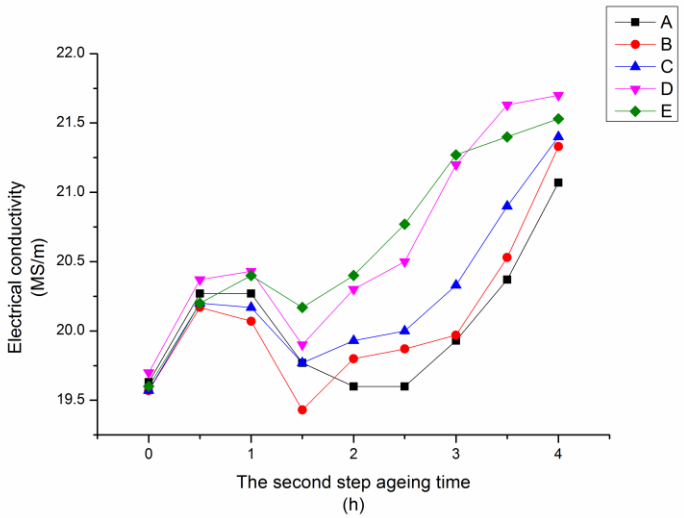

Figure 1. Influence of the second step ageing treatment on the evolution of electrical conductivity in the samples.

As shown in Fig.2a, in the sample A and B, three wave valleys are seen at 0.5h, 1.5h and 2.5h, respectively, accompanied by two wave crests at 1h and 2h, respectively. Compared to the sample A and B, less wave valleys are seen in the sample C, D and E in Fig.2b, and the locations of the wave valleys change. Before the second step ageing, the higher pre-strain led to higher Vickers-hardness, which might result from strain hardening. The Vickers-hardness of all the samples reached lowest at around 1.5h to 2h. Compared to the sample A, the Vickers-hardness of the sample B, C, D and E decrease after 3.5h.

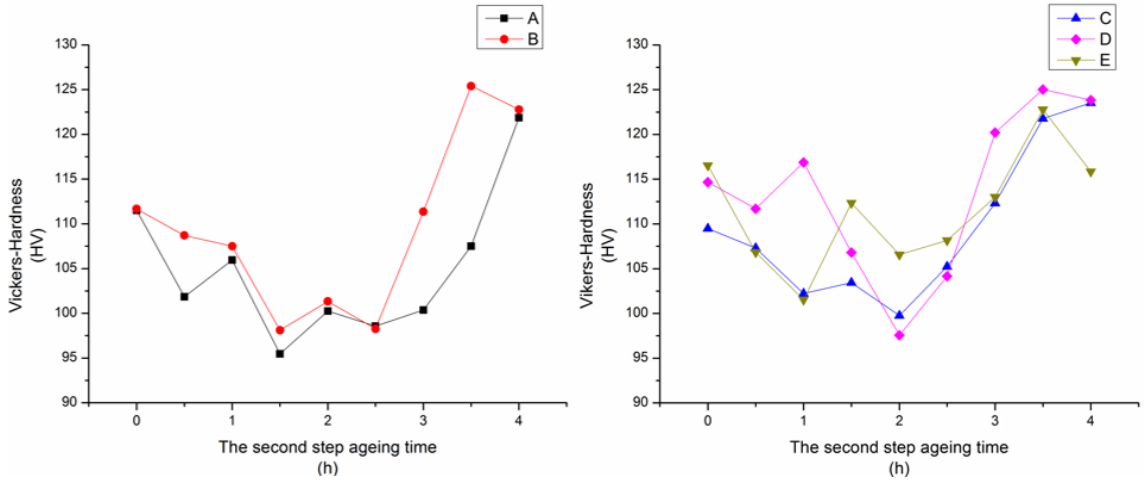

Figure 2. Influence of the second step ageing treatment on the evolution of Vickers-harness in the samples: (a) A and B; (b) C, D and E.

Fig.3a-b show two SAED patterns in <001>Al from the sample A at 0h, 0.5h second step ageing, respectively. And Fig.3c-e show three SAED patterns in <111>Al from the sample A at 1.5h, 2.5h and 4h of the second step ageing, respectively. The main strong diffraction spots are attributed to Al matrix. The weak sharp spots at {100} and {110} in Fig.3a-b and the weak sharp spots at {110} and {211} in Fig.3c-e results from Al3Zr dispersions [24, 25]. The weak spots at {1, (2n+1)/4, 0} positions in Fig.3a reflects spherical GPI zones form after the first step ageing [24, 26, 27], compared to none such weak spots in Fig.3b, indicating that GPI zones dissolve after 0.5h ageing. The sharp spots marked as the point A and B in Fig.3c locate at the positions neighboring 2/3{211} which are also seen in Fig.3d and e, and the same spots were also observed in Y. Duan's work [28] on A7N01-T4 Al alloy and in Y. C. Lin's work [29] on an Al-5.8Zn-2.3Mg-1.5Cu-0.21Cr, in which those spots were ascribed to GPII zones in their opinions. The weak spots marked as the point Cat neighboring {211} in Fig.3c are hard to distinguish at the similar positions in Fig.3d, indicating these weak spots are not formed by Al3Zr. The angle AOB measured three times for average is 69.735 degree, and the length ratio of OC to OA is about 1.129. Based on information above, a hypothesis was proposed that the spots at A, B and C were the consequence of a kind of face-centered cubic (fcc) precipitates, whose <011> zone axis was parallel to <111>Al. The SAED patterns in Fig.3c and d confirm the fcc unit cell of the precipitates a=0.347nm, and the fcc unit cell of Al matrix a=0.391nm. The weak spots at 2/3{220} and 2/3{211} shown in Fig.3e result from η' phases, and those weak spots around 2/3{220} and 2/3{211} result from η1 phases[25,30,31].

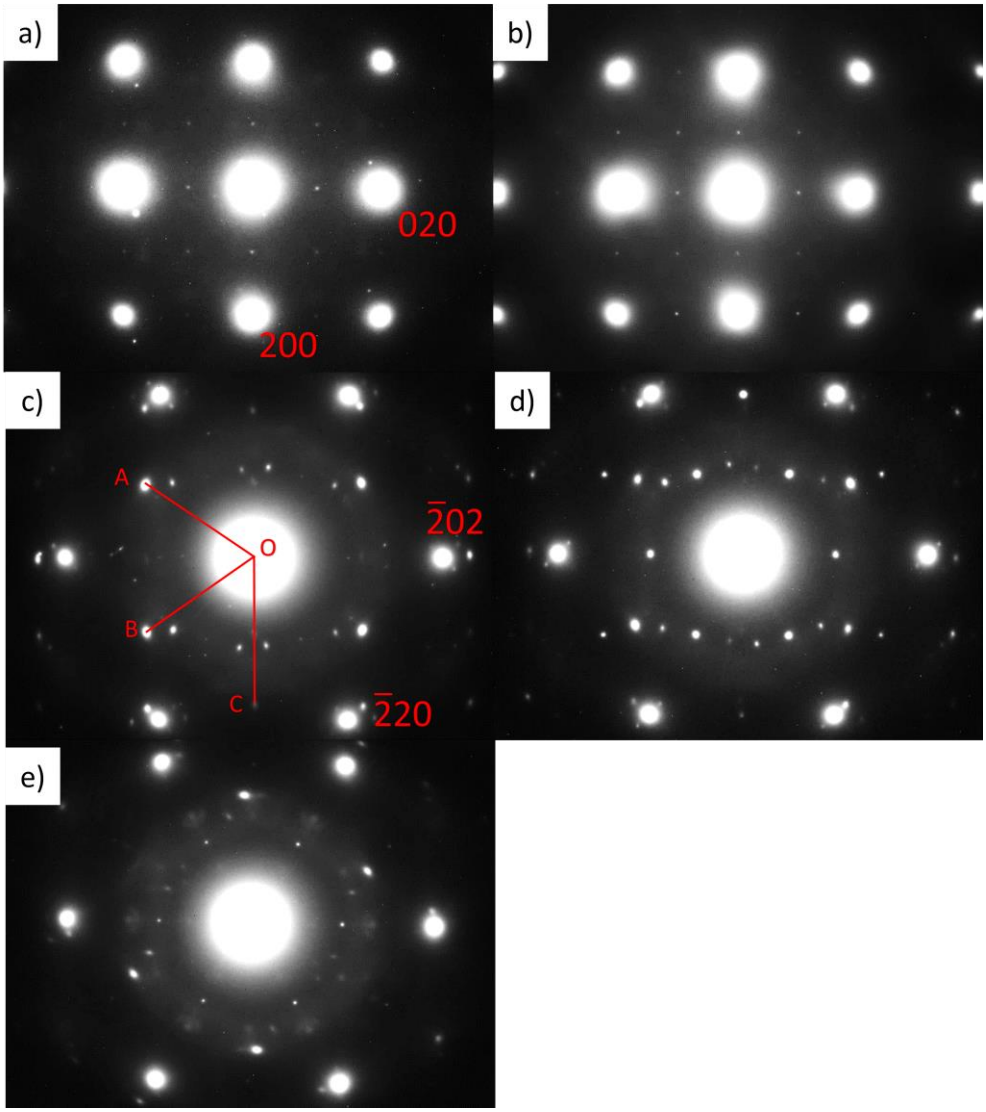

Figure 3. SAED patterns of the sample A at: (a) 0h; (b) 0.5h; (c) 1.5h; (d) 2.5h; (e) 4h of the second step ageing.

Fig.4a-f show TEM BF images in <011>Al zone axis from the sample A at 0h, 0.5h, 1.5h, 2.5h, 3h and 4h, respectively. As shown in Fig.4a, most nano scale precipitates are spherical, but some rod-shape precipitates can also be distinguished. And there are two kinds of precipitates seen in Fig.4a, one is clear coarser spherical or rod-shape precipitate, another one is blurred finer spherical precipitate. Compared to Fig.4a, the size of clear precipitates is larger and the blurred finer precipitates are disappear in Fig.4b, which may correspond to the weak spots at {1,(2n+1)/4,0} positions fading in Fig.3b. Most precipitates in Fig.4b-e are clear coarser spherical or rod-shape precipitates, and the long sides of the most rod-shape precipitates are vertical to g=[111]. It is telling that the precipitates in Fig.4d are denser than those in Fig.4c and e, possibly corresponding to the sharpest spots near 2/3{211} in Fig.3d. As shown in Fig.4f, those plate-shape or rod-shape precipitates at the size of about 10nm are distinguished as η' phases or η phases, corresponding to the spots seen at or near the position of 1/3{220}, 2/3{220} and 1/3{420} in Fig.3e.

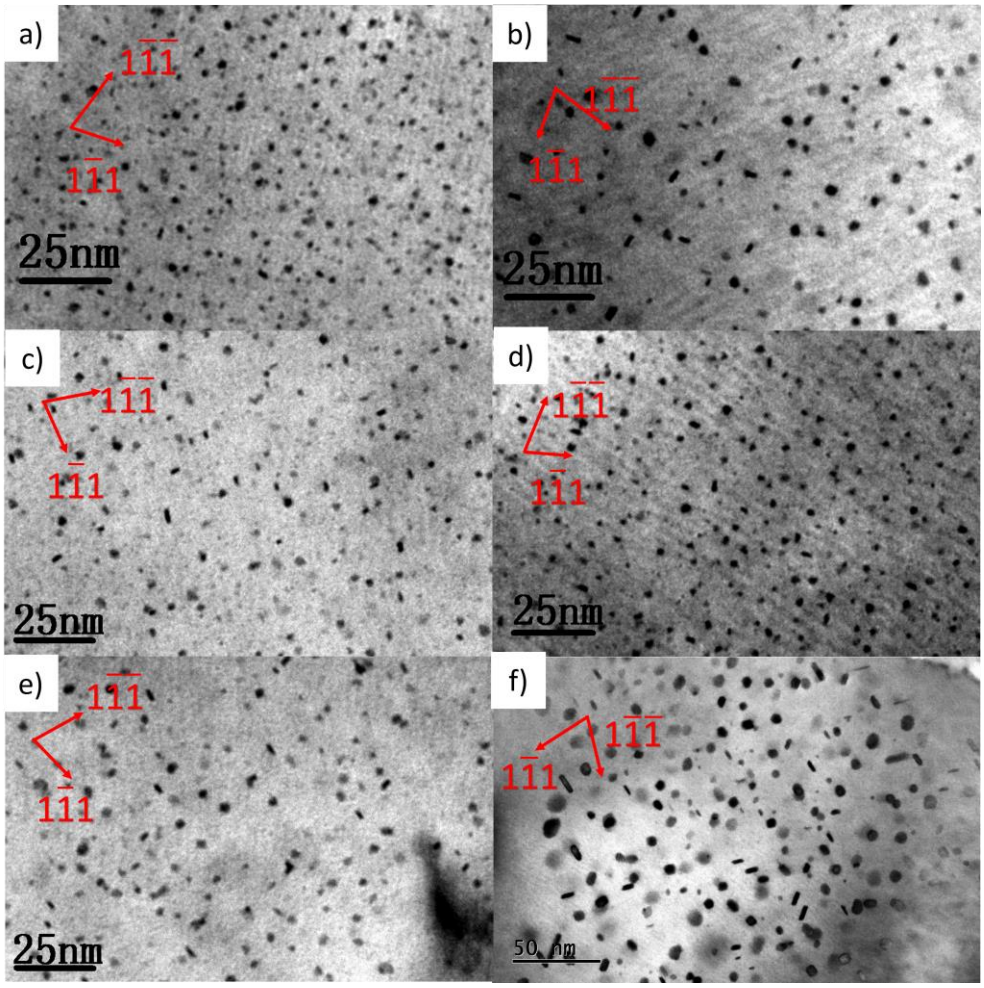

Figure 4. Typical BF images of the sample A at: (a) 0h; (b) 0.5h; (c) 1.5h; (d) 2.5h; (e) 3h; (f) 4h of the second step ageing.

Fig.5a-d show four SAED patterns in <111>Al from the sample D at 1h, 2h, 3.5h and 4h of the second step ageing, respectively. The spots near 2/3{211} can be seen in all the four SAED patterns in Fig.5, while the intensity changes during the second step ageing. The weak spots at and around n/3{220} and n/3{211} in Fig.5c and d result from η' phases and η1 phases, respectively[25,30,31]. More obvious spots resulted by η' phases and η phases (in the orientations η1, η2 and η4)[31] are seen in Fig.5d, compared to Fig.5c and Fig.3e.

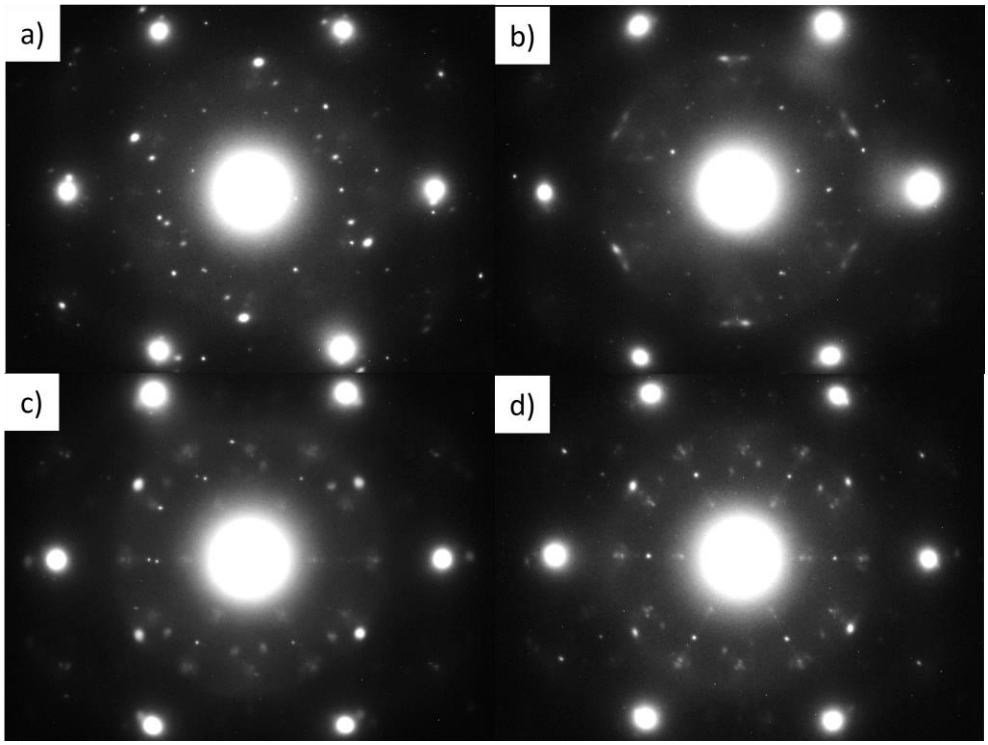

Figure 5. SAED patterns of the sample D at: (a) 1h; (b) 2h; (c) 3.5h; (d) 4h of the second step ageing.

Fig.6a-d show BF images in <011>Al zone axis from the sample D at 1h, 2h, 3.5h, 4h, respectively. From Fig.6a to b, the size of the clear coarser spherical or rod-shape precipitates decreases. In Fig.6b, the shaded above 10nm zones accompanied by the size of surrounding precipitates decreasing may be related to the transformation from the fcc precipitates to η' phases, which can also be seen at lower right corner in Fig.4e.

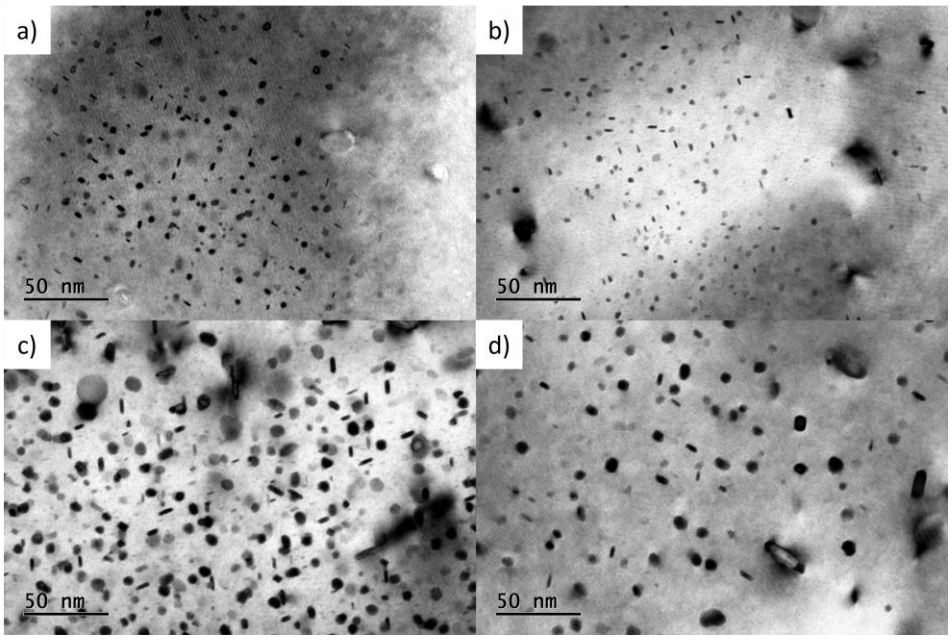

Figure 6. Typical BF images of the sample D at: (a) 1h; (b) 2h; (c) 3.5h; (d) 4h of the second step ageing.

Fig.7a-b show dislocations under the condition of g=[$\bar{1}11$] and similar thickness in the sample A and D before the second step ageing, respectively, since the sample A and D were mainly focused on for studying matrix precipitates during the second step ageing. The densities of the dislocations increase as the pre-strain increasing. In former works on dislocations in pre-strained 7xxx series alloys, the pre-strain was recognized as what led to the generation of the dislocation in general[14].

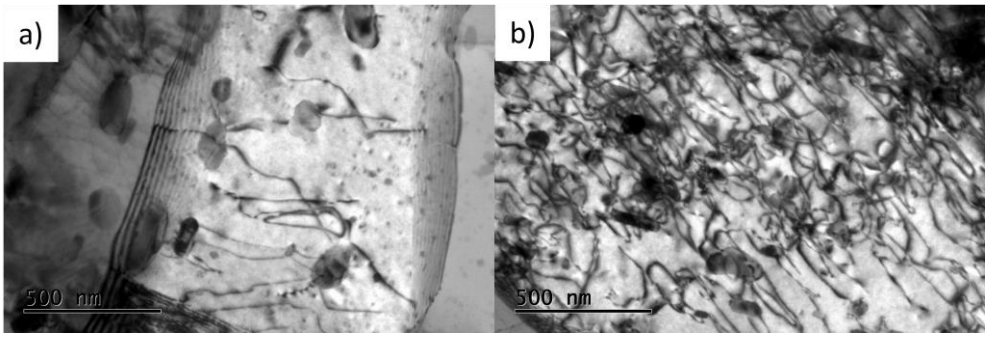

Figure 7. BF images of the sample: (a) A; (b) D.

The EXCO ratings of the five samples listed in Table.1 were rated based on the surface morphology after 48h immersion in EXCO solution of the five samples (as shown in Fig.8), respectively. The ratings were all ED, though the sample A is less corroded as shown in Fig.8a, compared to other samples. To distinguish the different EXCO resistance of the same EXCO rating of the five samples, a method by measuring the average thickness of EXCO products on longitudinal section were used in this work, and the results from at least three images for each example were listed in Table.1. The typical EXCO products in the sample A, C and D, which are brighter in contrast (due to their poor performance in electrical conductivity) and fusiform in shape, were shown in Fig.9 for examples. The average thickness of EXCO products in each sample was calculated in at least three SEM images and then was listed in Table.1.

Fig.10 shows grain boundaries precipitates of the five samples after the second step ageing. In this rolled Al-Zn-Mg alloy, due to the higher grain boundaries energy, the precipitates on HAGBs distributing discontinuously are coarser and prior corroded in EXCO tests, compared to those on low-angle grain boundaries or sub-grain boundaries. Therefore, the precipitates on HAGBs were focused on in this work. Based on the HAADF-STEM images of the five samples shown in Fig.10, the average coverage ratio and size of the η phases on HAGBs were calculated and listed in Table.1. The coverage ratio, which is defined as line fraction of total length of η phases in the direction of HAGB to total length of HAGB, increase as the pre-strain increase in general, and it seems the coverage ratio rapidly reaches about 50% since the pre-strain reaches 0.65% and remains around this value until the pre-strain reaches 7.50%. As for the size, it seems the sizes decrease as pre-strain increase generally.

Besides, the recrystallization fractions calculated from EBSD results in the five samples were also listed in Table.1, and the typical EBSD images were shown in Fig.11. But it seems the fractions of the five samples have little connection with pre-strain.

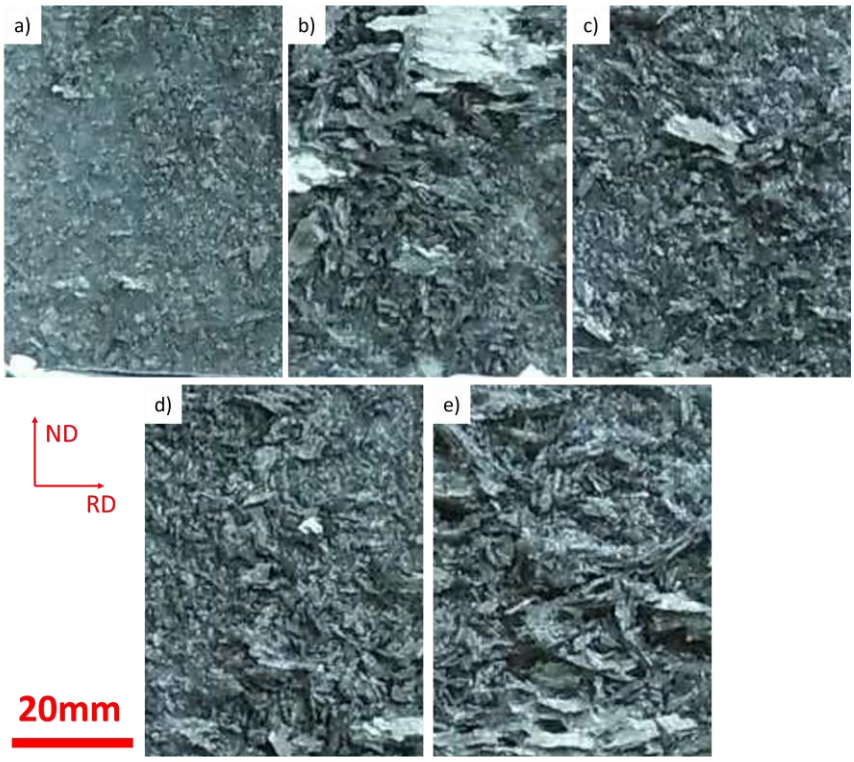

Figure 8. Surface morphology of the sample: (a) A; (b) B; (c) C; (d) D; (e) E.

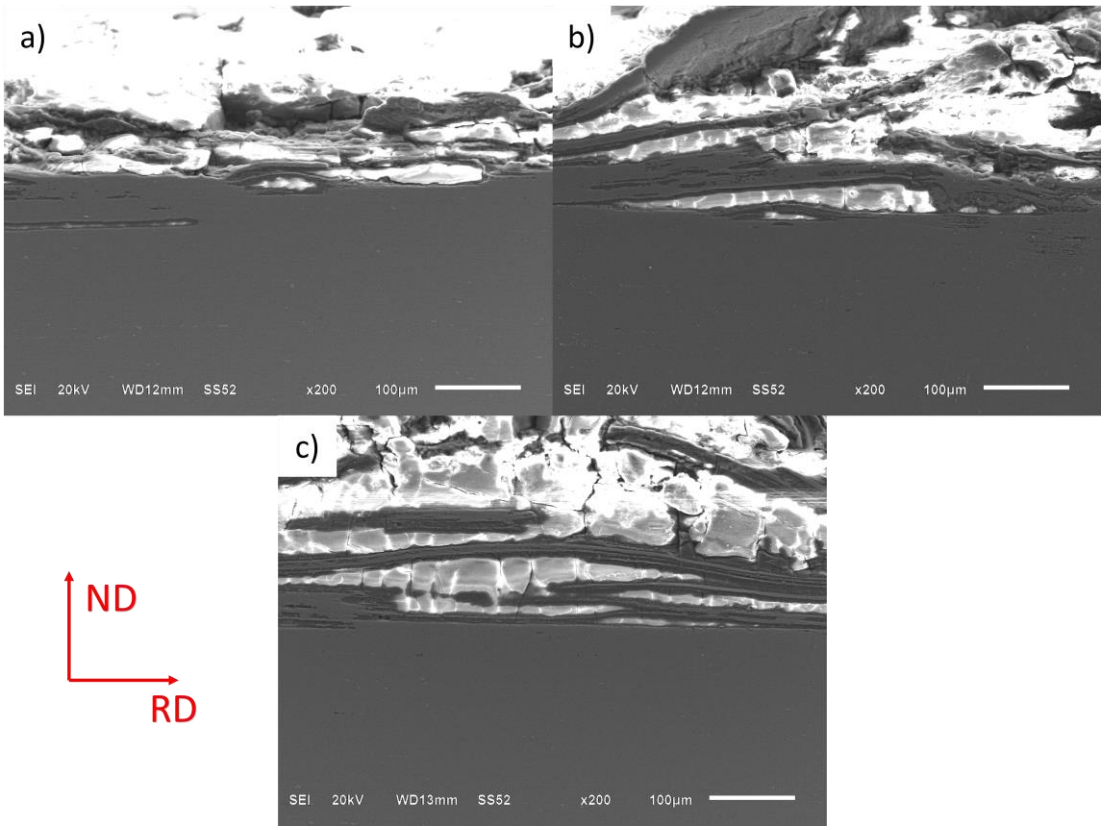

Figure 9. Typical SEM images of EXCO products on longitudinal section in the sample: (a) A; (b) C; (c) D.

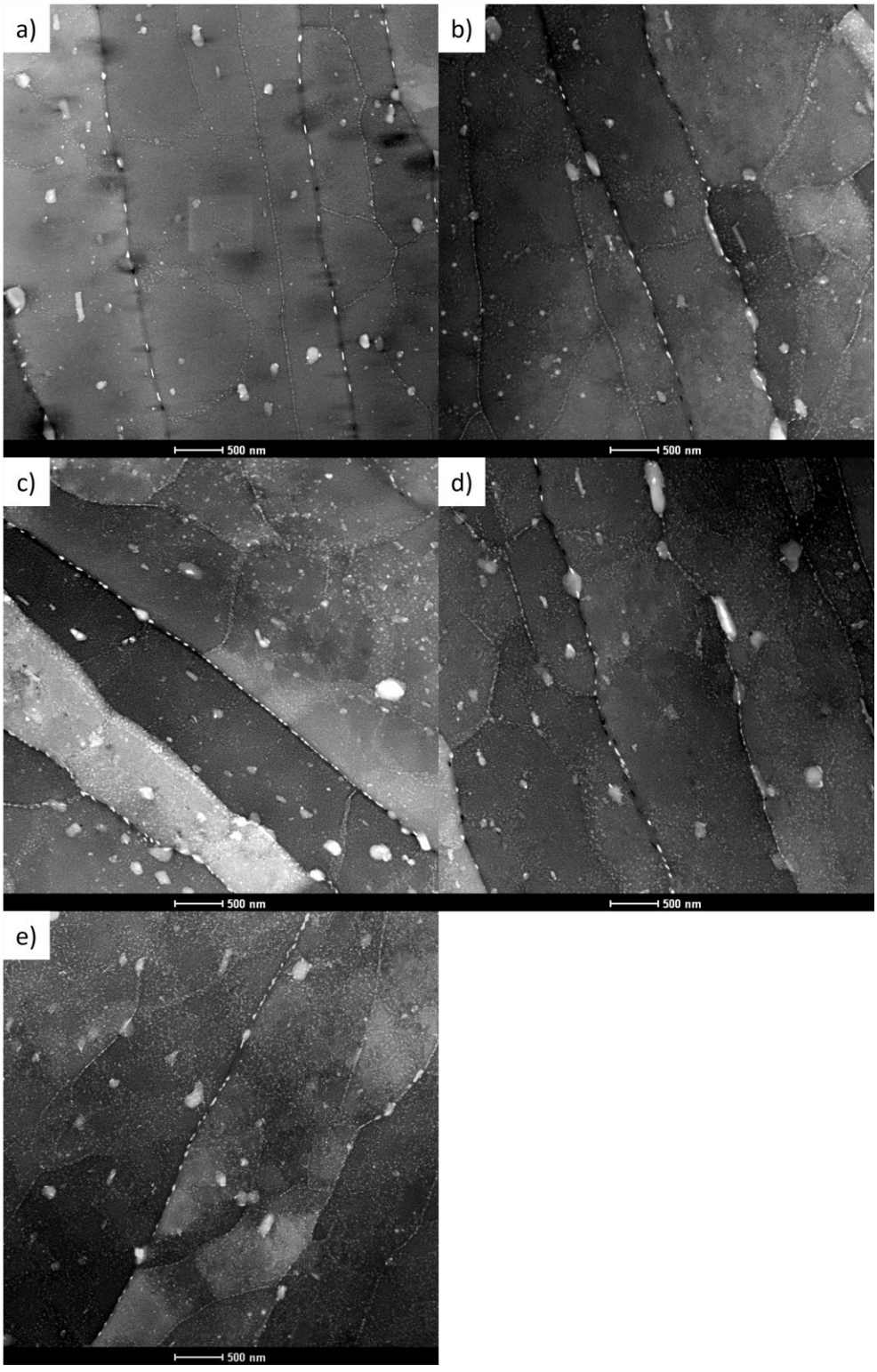

Figure 10. Coverage of η phases on HAGBs in HAADF-STEM images of the sample: (a) A; (b) B; (c) C; (d) D (e) E.

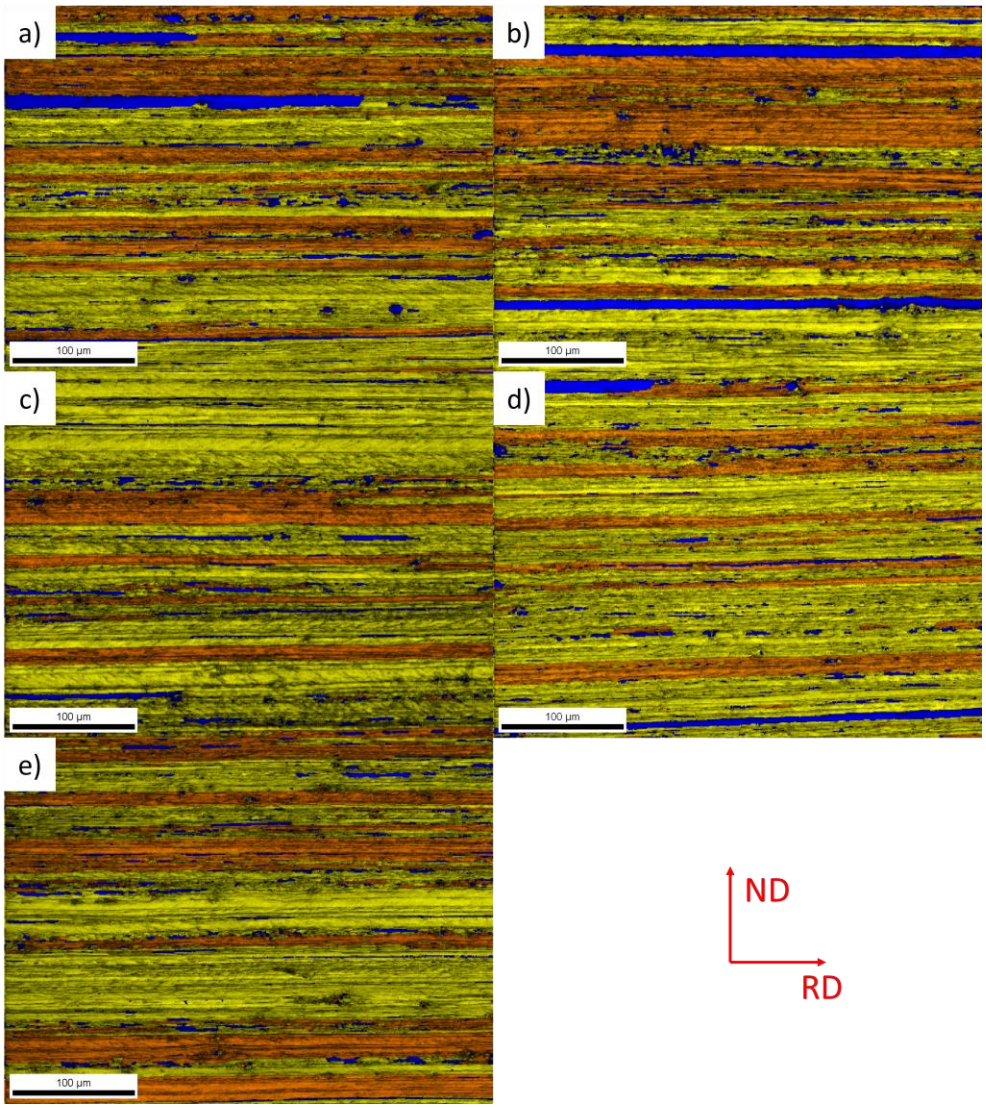

Figure 11. Typical calculated grain average disorientation images on longitudinal section by EBSD: (a) sample A; (b) sample B; (c) sample C; (d) sample D; (e) sample E.

Table 1. Results from images of SEM, HAADF-STEM and EBSD

Number	A	B	C	D	E
Exfoliation corrosion rating	ED	ED	ED	ED	ED
EXCO products thickness(μm)	25.2	36.6	54.8	63.5	48.8
Coverage ratio of η phases on HAGBs (%)	31.3	50.1	47	57	57.2
Average size of η phases on HAGBs(nm)	91.8	84.8	64.3	68.7	58.9
Recrystallization fraction (%)	8.7	7.5	5	6.9	4.3

4. Discussion

4.1. Precipitation

The similar fluctuations of electrical conductivity in the five samples during the second step ageing are seen in Fig.1, indicating the similar phases transformations were happened. Although in Al-Zn-Mg alloy the predominant factor influencing electrical conductivity is lattice distortion, the electrical conductivity decreases as GP zones precipitating in general. From 0h to 0.5h, it seems that some nano

scale blurred finer precipitates formed in first stage ageing dissolve, since electrical conductivity increases attributed to the size of those nano scale precipitates approximate to the wavelength of the free electrons in matrix during the electrical conductivity tests. These blurred precipitates are round in HR-TEM images shown in Fig.12a, which is consistent with the results of HR-TEM images of an Al-Zn-Mg-Cu alloy aged for 7h at 115℃ from the work of Z. H. Li [30]. The first transformation from 0h to 0.5h may be the dissolution of GPI zones corresponding to the transformation shown in BF images from Fig.4a to Fig.4b, which is proved by disappearing of weak patterns at the positions of {1,(2n+1)/4,0}. J. C. Werenskiold [31] summarized former works as that GPI zones either dissolved or transformed into η' phases at above the GP zones solvus in Al-Zn-Mg alloys, which accorded with the transformation happened from 0h to 0.5h in this work.

Hardening obtained in Al alloys mainly depends on metallic system involved and the volume fraction and size of main hardening particles [24]. In precipitation hardening Al-Zn-Mg alloys, solution hardening also have effect on hardness of Al matrix. During this stage, the Vickers-hardness of all the samples decrease in the first 0.5h, which may be dominantly attributed to that the precipitation hardening of GPI zones is more effective than the solution hardening resulted by GPI zones fading.

The second transformation may start from 0.5h or 1h until different time in different samples, such as, 2.5h in the sample A and 2h in the sample D. It seems some small precipitates at the size of about 5nm are precipitated from matrix during this stage as shown in Fig.4d. Actually, the precipitates in BF images including spherical ones and rod-shaped ones (whose longer sides are parallel to {111} Al) indicate there are some precipitates formed on the {111} plane of Al matrix. Moreover, compared to Fig.3c, the sharper patterns at the positions neighboring 2/3{211} and {211} shown in Fig.3d indicate a kind of precipitates whose <011> orientation is parallel to the <111> orientation of Al matrix increase from 1.5h to 2.5h. Consequently, it seems the rod-shaped precipitates in the bright field images are formed on the {111} planes of Al matrix which are parallel to the specific <011> zone axis of the images, while some of the spherical ones are projections of themselves formed on the {111} planes of Al matrix which are not parallel to the specific <011> zone axis. Therefore, it is reasonable to ascribe the spots near 2/3{211} to those rod-shaped precipitates and part of spherical precipitates. Moreover, these precipitates were not only found after the first transformation finished but were also distinguished in the sample A before the second step ageing (shown in Fig.12a and b), indicating these precipitates were more stable than GPI at the temperature of the second step ageing.

In J. Z. Liu's work[33], HAADF-STEM was used to observe the atoms arrangement of the similar precipitates named GP-η' and GP-ηp in the peak-aged 7N01 alloy and 7055 alloy, respectively, and their results showed these precipitates were both Zn-rich clusters on {111}Al. And the Marinara model of GP-ηp precipitate [34] showed a similar microstructure of Zn-rich clusters on {111} Al. In their investigations on GP-η' or GP-ηp, these phases were made up mainly of a framework of Zn atoms. According to the results (the fcc unit cell, a=0.347nm) in this work, only Zn atoms planes can fit in the unit cell parameter on the condition that Mg atoms are larger than Al atoms. It seems the fcc precipitates in this work are also Zn-rich clusters on {111} Al and were made up of a similar framework. In K. Stiller's work, the GPII zones in an Al-2.30Zn-1.38Mg alloy were described as a few atoms layers thick on {111}-planes, leading to six weak spots at the positions near 2/3{220} in SAED patterns of [111] projection. As mentioned above, the spots from the fcc precipitates in this work, Y. C. Lin's work or Yi Duan's works locate at the different positions, compared to the spots from GPII zones in K. Stiller's alloy containing less Zn. Besides, the HR-TEM images as shown in Fig.12 and Z. H. Li's work[30] pointed out the thickness of this kind of Zn-rich clusters along [111]Al were approximate 1nm, showing big difference with HR-TEM images of GPII in L. K. Berg's work[26]. So it is more reliable to classify the fcc precipitates and GP-η' or GP-ηp together, rather than GPII zones.

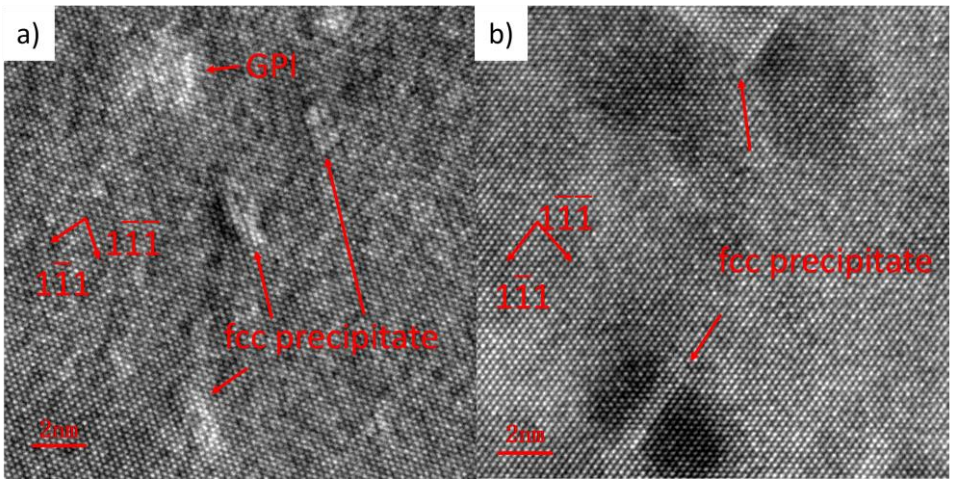

Figure 12. HR-TEM images in [011]Al zone axis of (a)the first selected area and (b)the second selected area in the sample A before the second step ageing.

The software was used for simulating the different intensities between {200} and {111} of fcc precipitates themselves when incident electron beam was vertical to (111) Al and the thickness of precipitates were 1nm (measured in Fig.4d). Results were shown in Fig.13, indicating rotating 9.81° on [01-1] zone axis of fcc precipitates could lead to weak {200} patterns. As shown in Fig.13b, the angle between {111} is 68.74°, which accords the results measured in Fig.3c to e. So the [011] zone axis of the fcc precipitates may not be perfectly parallel to [111]Al but have a 9.81° deviation in particular direction.

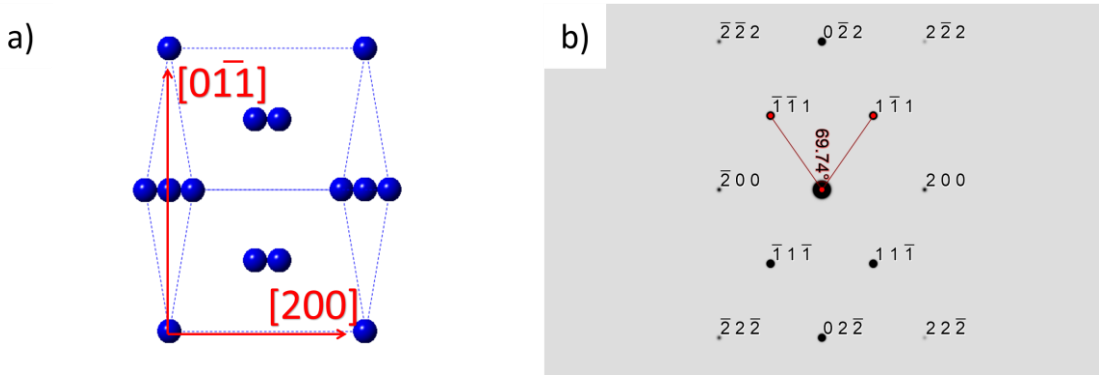

Figure 13. Unit cell of fcc precipitates after 9.81 °rotation in (a) and its corresponding SAED patterns simulation in (b).

During this stage, the Vickers-hardness of all the samples decrease in general but some fluctuations still exist. Those fluctuations may be related to experimental errors caused by measuring or natural ageing hardening happened after unfinished artificial ageing. Compared to decrease of the hardness ascribed to the dissolution of GPI zones, the decrease in this stage, which is resulted from this kind of precipitates forming, indicate this kind of precipitates have little effect on hardening the Al-Zn-Mg alloy used in this work, even cannot make up the lost hardness caused by the decrease of solution concentration.

The third transformation attributed to the formation of η' phases and η phases may follow the end of the second transformation, indicating the evolution from the fcc precipitates to η' phases may exist. At the beginning of this stage, as shown in Fig.4e and Fig.6b, some shaded zones are seen, which may lead to the weak shaded patterns neighboring 2/3{211} in Fig.5b. In others former work,

these weak patterns were attributed to a kind of precipitates named GPII zones, which is also rod-shaped in bright field images. Then, the η' phases or η phases seen in Fig.3e and Fig.5c form, and their patterns are seen in Fig.4f and Fig.6c, respectively. The electrical conductivity of all the samples increase rapidly as η' phases and η phases forming because of the main solute atoms in Al matrix decreasing as the semi-coherent η' phases and the incoherent η phases forming. Compared to the rapid increase of Vickers-hardness in the un-strained sample A, the hardness in pre-strained samples firstly increase rapidly and decrease after 3.5h which is the consequence of the average size of the η' phases or the η phases increasing from 7.3nm to 11.5nm as shown in Fig.5c and Fig.5d. The transformation from η' phases to η phases is inevitable because the second step ageing temperature is high.

Above all, the pre-strain before ageing accelerated the precipitation in this alloy. Furthermore, 4h of the second step ageing may be not enough for un-strained sample to acquire max hardness, but excessive for pre-strained sample. This acceleration led by pre-strain may be ascribed to the dislocations produced by pre-strain as shown in Fig.7. Moreover, the precipitation hardening from GPI zones is more effective than that from the fcc precipitates whose increase in density leads to decrease of Vickers-hardness.

4.2. EXCO resistance

In previous work, the coverage ratio of η phases on HAGBs and the fraction of recrystallization and HAGBs were focused on to investigate the effect of microstructure on EXCO resistance in the same composition Al-Zn-Mg alloy used in this work. Besides, in former works of other scholars, the size and distribution of η phases on HAGBs were also focused on. Therefore, in this work, these factors were measured, calculated and discussed to illustrate the effect of pre-strain on EXCO resistance.

To elucidate the relationship between these series of results (as shown in Table.1) with the EXCO behaviors of the five samples, the scaling factors obtained by dividing the results by the maximum values among the series of results were made into line chart as shown in Fig.14. Obviously, no line of the scaling factors of any series of results perfectly accords with the line of the scaling factors of the EXCO products thickness.

However, compared to other lines, the line of the scaling factors of the coverage ratio accords with the line of the EXCO products thickness better, indicating the coverage ratio may be the predominant factor effecting EXCO resistance. There are two investigations mentioning coverage ratio before, and coverage ratio was firstly proposed [35] for explaining results which cannot be explained by size or distribution of η phases on HAGBs. In Marlaud's work investigating EXCO mechanism on 7449 Al alloy [35], conclusion was drawn as the EXCO sensitivities increase as the coverage ratio increase. And they also found η phases on HAGBs were prior corroded during 30s immersion in corrosion solution, compared to matrix and precipitates free zones. Moreover, in S. D. Liu's work [36] on EXCO mechanism in 7055 Al alloy, the coverage ratio was also found as the main factor influence EXCO resistance, which was explained as high coverage ratio increased the area of attacked regions during immersion. Combining above results with the results from this work, it can be therefore summarized that the high coverage ratio leads to large prior corroded area on HAGBs, which deteriorate the resistance against EXCO.

As for the size, in our previous work and works of Maraud [35] and S. D. Liu[36], it seemed that the size had little effect on EXCO resistance, which is contradictory with the results in G. S. Peng's[37], S. Y. Chen's[38] and J. R. Zuo's [39] investigations on the influence of GBPs on EXCO behavior. Their works were carried out in a specially developed Al-Zn-Mg-Cu alloy, 7085 Al alloy and 7055 Al alloy, respectively, revealing coarser and discontinuous η phases resist EXCO effectively. In this work, the scaling factors line of the size accords with the line of EXCO products thickness before 1.97% pre-strain but not after that. Based on the results above, it is unconvincing to conclude coarser η phases resist EXCO better.

Considering the fraction of recrystallization, it was reported in our former works that recrystallized grains were susceptible to EXCO when the EXCO ratings of the samples ranged from P to EB. While in this work, it is evident the scaling factors line of the recrystallization fraction does not accord with the line of EXCO product thickness, indicating the recrystallization fraction has little impact on the EXCO resistance of the five samples with the EXCO ratings of ED. Which is to say, the recrystallization fraction is not the predominant factor effecting EXCO resistance when the EXCO resistance is low.

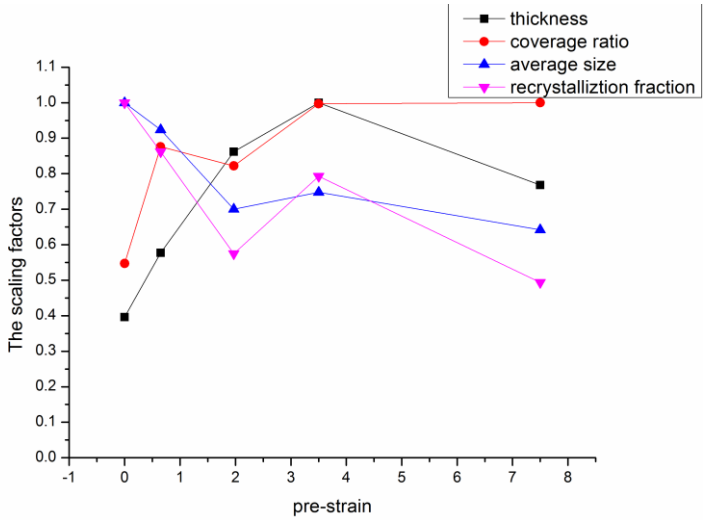

Figure 14. Trend of the concerned factors and the EXCO susceptibilities during pre-strain increasing.

5. Conclusion

The combination of behavior tests and microstructure examination was conducted in this investigation to elucidate the precipitation during the second step ageing and the predominant factor influencing EXCO resistance in this Al-4.5Zn-1.2Mg alloy, and so provided insight into the effect of pre-strain on precipitation and EXCO resistance, which was concluded as follows:

(1) The increased dislocation density ascribed to pre-strain leads to acceleration of matrix precipitation.

(2) The most possible precipitation sequence during the two step ageing applied on this alloy is: SSS-GPI zones precipitation-GPI dissolution; SSS-fcc precipitation-η' phases or η phases forming. And the nano fcc precipitates whose <011> zone axis is nearly parallel to the <111>Al deteriorate the hardness of Al matrix.

(3) The increased pre-strain from 0% to 3.41% leads to the increased susceptibility to EXCO, but slightly decrease were seen at 7.50% pre-strain. The coverage ratio of η phases on HAGBs increasing as pre-strain increase generally may play the dominant role in effecting EXCO resistance, rather than the average size or the recrystallization fraction.

Acknowledgments

This work was financially supported by National Natural Science Foundation of China (Grant No. 51501015) fund.

References

[1] Z. W. Du, Z. M. Sun, B. L. Shao, T. T. Zhou, C. Q. Chen, Quantitative evaluation of precipitates in an Al-Zn-Mg-Cu alloy after isothermal aging, J. Materials Characterization 56

(2006) 121-126.
[2] Z. W. Du, T. T. Zhou, C. Q. Chen, P. Y. Liu, B. Z. Dong, Quantitative analysis of precipitation in an Al-Zn-Mg-Cu-Li alloy, J. Materials Characterization 55 (2005) 75-82.
[3] L. B. Jin, G. Zhao, Z. H. Feng, L. Y. Lu, Medium strength and wieldable Al-Zn-Mg alloys on high speed train, J. Light Alloy Fabrication Technology 38 (2010) 47-51. (in Chinese)
[4] B. Li, X. M. Wang, H. Chen, J. Hu, C. Huang, G. Q. Gou, Influence of heat treatment on the strength and fracture toughness of 7N01 aluminum alloy, J. Journal of Alloys and Compounds 678 (2016) 160-166.
[5] Y. L. Wang, H. C. Jiang, Z. M. Li, D. S. Yan, D. Zhang, L. J. Rong, Two-stage double peaks ageing and its effect on stress corrosion cracking susceptibility of Al-Zn-Mg alloy, J. Journal of Materials Science & Technology (2017) in press
[6] S. D. Ji, X. C. Meng, R. F. Huang, L. Ma, S. S. Gao, Microstructures and mechanical properties of 7N01-T4 aluminum alloy joints by active-passive filling friction stir repairing, J. Materials Science & Engineering A 664 (2016) 94-102.
[7] J. S. Robinson, W. Redington, The influence of alloy composition on residual stresses in heat treated aluminum alloys, J. Materials Characterization 105 (2015) 47-55.
[8] J. S. Robinson, D. A. Tanner, C. E. Truman, A. M. Paradowska, R. C. Wimpory, The influence of quench sensitivity on residual stresses in the aluminium alloys 7010 and 7075, J. Materials Characterization 65 (2012) 73-85.
[9] Z. Zhang, Y. F. Yang, L. Li, B. Chen, H. Tian, Assessment of residual stress of 7050-T7452 aluminum alloy forging using the contour method, J. Materials Science & Engineering A 644 (2015) 61-68.
[10] N. Chobaut, D. Carron, S. Arsene, J. –M. Drezet, Quench induced residual stress prediction in heat treatable 7xxx aluminium alloy thick plates using Gleeble interrupted quench tests, J. Journal of Materials Processing Technology 222 (2015) 373-380.
[11] Michael B. Prime, Michael R. Hill, Residual stress, stress relief, and inhomogeneity in aluminum plate, J. Scripta Materialia 46 (2002) 77-82.
[12] S. Y. Zhang, Y. X. Wu, H. Gong, A modeling of residual stress in stretched aluminum alloy plate, J. Journal of Materials Processing Technology, 212 (2012) 2463-2473.
[13] D. Wang, Z. Y. Ma, Effect of pre-strain on microstructure and stress-corrosion cracking of over-aged 7050 aluminum alloy, J. Journal of Alloys and Compounds 469 (2009) 445-450.
[14] N. M. Han, X. M. Zhang, S. D. Liu, B. Ke, X. Xin, Effects of pre-stretching and ageing on the strength and fracture toughness of aluminum alloy 7050, J. Materials Science and Engineering A, 528 (2011) 3714-3721.
[15] Ramazan Kacar, Kemal Guleryuz, Effect of quenching rate and pre-strain on the strain ageing behaviors of 7075 aluminum alloys, J. Materials Research 18 (2015).
[16] L. W. Quan, G. Zhao, S. Gao, Barry C. Muddle, Effect of pre-stretching on microstructure of aged 2524 aluminium alloy, J. Transactions of Nonferrous Metals Society of China 21 (2011) 1957-1962.
[17] B. I. Rodgers, P. B. Prangnell, Quantification of the influence of increased pre-stretching on microstructure-strength relationships in the Al-Cu-Li alloy AA2195, J. Acta Materialia 108 (2016) 55-67.
[18] Y. Li, Z. Y. Liu, S. Bai, L. H. Lin, L. F. Gao, Effects of pre-strain on exfoliation corrosion behavior in Al-Cu-Mg alloy, J. Journal of Materials Engineering and Performance 21 (2012) 1479-1484.
[19] Z. H. Li, B. Q. Xiong, Y. A. Zhang, B. H. Zhu, F. Wang, H. W. Liu, Investigation on strength, toughness and microstructure of an Al-Zn-Mg-Cu alloy pre-stretched thick plates in various ageing tempers, J. Journal of Materials Processing Technology 209 (2009) 2021-2027.
[20] C. Cao, D. Zhang, L. Z. Zhuang, J. S. Zhang, Improved age-hardening response and altered precipitation behavior of Al-5.2Mg-0.45Cu-2.0Zn(wt%) alloy with pre-ageing treatment, J. Journal of Alloys and Compounds 691 (2017) 40-43.

[21] Y. C. Lin, J. L. Zhang, G. Liu, Y. J. Liang, Effects of pre-treatments on ageing precipitates and corrosion resistance of a creep-aged Al-Zn-Mg-Cu alloy, J. Materials & Design 83 (2015) 866-875.
[22] D. Feng, X. M. Zhang, S. D. Liu, T. Wang, Z. Z. Wu, Y. W. Guo, The effect of pre-ageing temperature and retrogression heating rate on the microstructure and properties of AA7055, J. Materials Science & Engineering A 588 (2013) 34-42.
[23] ASTM G34-01(2013), Standard Test Method for Exfoliation Corrosion Susceptibility in 2XXX and 7XXX Series Aluminum Alloys (EXCO Test), ASTM International, West Conshohocken, PA, 2013, www.astm.org.
[24] X. G. Fan, D. M. Jiang, Q. C. Meng, Z. H. Lai, X. M. Zhang, Characterization of precipitation microstructure and properties of 7150 aluminium alloy, J. Materials Science and Engineering A 427 (2006) 130-135.
[25] K. Stiller, P.J. Warren, V. Hansen, J. Angenete, J. Gjønnes, Investigation of precipitation in an Al–Zn–Mg alloy after two-step ageing treatment at 100° and 150°C, J, Materials Science and Engineering A 270 (1999) 55-63.
[26] L. K. Berg, J. Gjonnes, V. Hansen, X. Z. Li, M. Knutson-Wedel, G. Waterloo, D. Schryvers and L. R. Wallenberg, GP-zones in Al-Zn-Mg alloys and their role in artificial aging, J. Acta Materialia 49 (2001) 3443-3451.
[27] T. Engdahl, V. Hansen, P. J. Warren, K. Stiller, Investigation of fine scale precipitates in Al-Zn-Mg alloys after various heat treatments, J. Materials Science and Engineering A 327 (2002) 59-64.
[28] Yi Duan, Jijin Xu, Jingyao Chen, Chun Yu, Junmei Chen, Hao Lu, The effects of heat treatment on the microstructure and cyclic behavior of A7N01-T4 aluminum alloy, J, Materials Characterization, Accepted manuscript.
[29] Y. C. Lin, J. L. Zhang, M. S. Chen, Evolution of precipitates during two-stage stress-ageing of an Al-Zn-Mg-Cu alloy, J. Journal of Alloys and Compounds 684 (2016) 177-187.
[30] Z. H. Li, B. Q. Xiong, Y. A. Zhang, B. H. Zhu, F. Wang, H. W. Liu, Investigation of microstructural evolution and mechanical properties during two-step ageing treatment at 115 and 160°C in an Al-Zn-Mg-Cu alloy pre-stretched thick plate, J. Materials Characterization 59 (2008) 278-282.
[31] J. C. Werenskiold, A. Deschamps, Y. Brechet, Characterization and modeling of precipitation kinetics in an Al-Zn-Mg alloy, J. Materials Science and Engineering A 293 (2000) 267-274.
[32] A. Kverneland, V. Hansen, G. Thorkildsen, H. B. Larsen, P. Pattison, X. Z. Li, J. Gjønnes, Transformations and structures in the Al–Zn–Mg alloy system: A diffraction study using synchrotron radiation and electron precession, J, Materials Science and Engineering A 528 (2011) 880-887.
[33] J. Z. Liu, J. H. Chen, Z. R. Liu, C. L. Wu, Fine precipitation scenarios of AlZnMg(Cu) alloys revealed by advanced atomic-resolution electron microscopy study Part II: Fine precipitation scenarios in AnZnMg(Cu) alloys, J. Materials Characterization 99 (2015) 142-149.
[34] Sigurd Wenner, Jesper Friis, Calin D. Marioara, Randi Holmestad, Precipitation in a mixed Al-Cu-Mg/Al-Zn-Mg alloy system, J. Journal of Alloys and Compounds 684 (2016) 195-200.
[35] T. Marlaud, B. Malki, C. Henon, A. Deschamps, B. Baroux, Relationship between alloy composition, microstructure and exfoliation corrosion in Al-Zn-Mg-Cu alloys, J. Corrosion Science 53 (2011) 3139-3149.
[36] S. D. Liu, B. Chen, C. B. Li, Y. Dai, Y. L. Deng, X. M. Zhang, Mechanism of low exfoliation corrosion resistance due to slow quenching in high strength aluminium alloy, J. Corrosion Science 91 (2015) 203-212.
[37] G. S. Peng, K. H. Chen, S. Y. Chen, H. C. Fang, Influence of dual retrogression and re-aging temper on microstructure, strength and exfoliation corrosion behavior of Al-Zn-Mg-Cu alloy, J. Transactions of Nonferrous Metals Society of China 22 (2012) 803-809.
[38] S. Y. Chen, K. H. Chen, G. S. Peng, L. Jia, P. X. Dong, Effect of heat treatment on strength,

exfoliation corrosion and electrochemical behavior of 7085 aluminium alloy, J. Materials and Design 35 (2012) 93-98.

[39] J. R. Zuo, L. G. Hou, J. T. Shi, H. Cui, L. Z. Zhuang, J. S. Zhang, Effect of deformation induced precipitation on dynamic aging process and improvement of mechanical/corrosion properties AA7055 aluminum alloy, J. Journal of Alloys and Compounds 708 (2017) 1131-1140.